Numerical simulation of the margination of platelets in the microvasculature

By H. Zhao AND E. S. G. Shaqfeh

1. Motivation

The concentration of platelets near vessel walls is a critical factor in the initial formation of a hemostatic plug and thrombosis. As the predominant non-liquid blood constituent, erythrocytes (or red blood cells, RBCs) occupy 36% to 53% of the blood volume (Kratz *et al.* 2004). The number density of platelets is about 1/10 of the RBCs, and their size (2-4μm in diameter) is significantly smaller than that of RBCs (about 8μm diameter). Hence the axial transport and lateral motion of platelets is heavily influenced by the distribution and kinematics of red cells. Known as the famous Fahraeus–Lindquist effect (Fahraeus & Lindqvist 1931), RBCs migrate toward the center of the vessel, thus leaving a near-wall cell-depleted layer where the platelets tend to concentrate.

The near-wall concentration of platelets and particles of similar sizes, as well as the necessary role of RBCs during the margination process, has been confirmed in experiments (Tilles & Eckstein 1987; Yeh & Eckstein 1994), though a detailed description is still unavailable. From their platelet adhesion experiments, Aarts et al (Aarts *et al.* 1986) fit the effective platelet diffusivity to a power law with respect to the mean flow shear, whereas the exponent is found to depend strongly on the hematocrit. The effective wall normal diffusivity of platelet migration is several orders of magnitude higher than their intrinsic Brownian diffusivity, and is considered to be a shear-induced diffusivity due to the hydrodynamic interactions between the platelets and RBCs (Tilles & Eckstein 1987; Yeh & Eckstein 1994). It is well known that in a rigid particle flow, the particle–particle collisions cause lateral movements; the frequency and intensity of these collisions determine the effective diffusivity of particles (Eckstein *et al.* 1977; Leighton & Acrivos 1987; Nott & Brady 1994). The situation is much more complicated in blood as RBCs are closely packed so that the cell–cell interactions occur continuously in time, with nearby cells gliding smoothly over each other. It is hence difficult to define any distinctive collision events that would lead to the scaling law of diffusivity with shear rate and particle size.

Because of the dominant RBC volume fraction and their larger size, the existence of platelets apparently does not alter the overall flow characteristics in any significant way. Moreover, the hydrodynamic interaction between the RBCs and platelets is expected to be dominated by the former, and the much smaller platelets mainly sample the velocity fluctuations due to the interactions between red cells. These ideas are examined in our present numerical simulation of a pressure-driven blood flow in a channel between two flat plates, where the hydrodynamic interactions between RBCs, platelets, and walls are solved fully-coupled by a boundary integral method. Focusing on the physical mechanism of platelet margination, we investigate the cellular flow's wall normal velocity fluctuation, velocity autocorrelation, and the diffusive spreading of passive non-Brownian tracers and platelets, with particular emphasis on the scaling of these quantities with wall shear rate $\dot{\gamma}_W$.

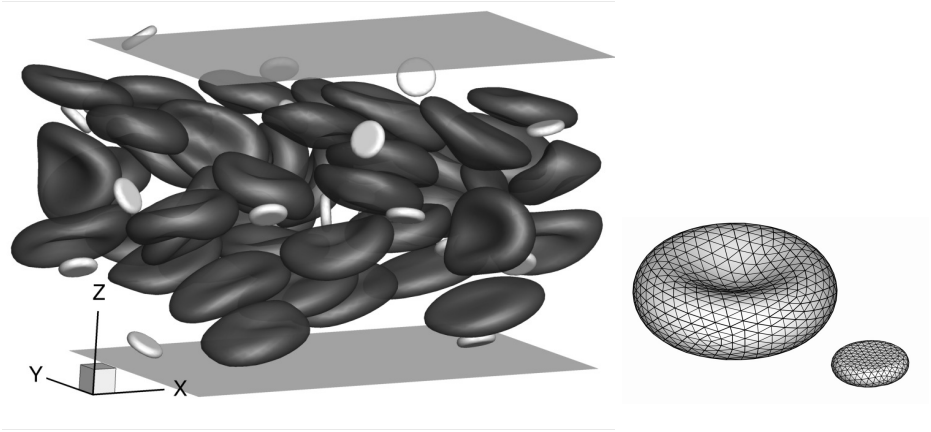

FIGURE 1. Left: simulated red blood cells and platelets in a channel flow. Right: the unstructured surface mesh used.

2. Numerical methods

Though the whole blood behaves as a non-Newtonian complex fluid (Chien *et al.* 1966), the fluid phase of the blood is essentially Newtonian. In small vessels, the flow is Stokesian due to the nearly zero Reynolds number, and can be solved by the boundary integral equation method (Pozrikidis 1992). Besides its rigorousness and superior accuracy, the boundary integral equation (BIE) method is particularly suitable here by obviating the difficult task of meshing the three-dimensional extracellular space that not only has very complex geometry but also deforms continuously in time.

As shown in Figure 1, the flow is between two infinite flat plates with normal direction along z, and is periodic in x and y. We apply a background velocity $\langle \mathbf{u} \rangle$ in the x direction as the flow driving force, and $\langle \mathbf{u} \rangle$ is the volume-averaged velocity in the computational domain. This is equivalent to applying a mean pressure gradient, and the relation between the two depends on the flow configuration. In our simulation, after the red cell distribution reaches steady state, the relative pressure fluctuations are always less than 1%.

The RBCs are modeled as massless elastic membranes with bending stiffness, so the residual stress from deformation must always be balanced by the hydrodynamic traction force acting on the membrane. This fact constitutes the starting point of forming the boundary integral equation to solve their surface velocities—a now standard procedure (Pozrikidis 2003). The platelets, on the other hand, are much stiffer than RBCs, and are modeled as rigid discoids since we have also assumed that these platelets are not "activated" and do not possess any complex surface features (Michelson 2006). Their rigid body motions are solved by an indirect double-layer BIE formulation (Pozrikidis 1992). On the vessel walls, we explicitly solve the hydrodynamic friction force that exactly enforces the no-slip condition there.

To derive the BIE for the full system, we first define the Stokes flow single-layer and double-layer integral operators on a closed surface D to be

$$(\mathbf{N}_D \boldsymbol{\psi})_j(\mathbf{x}_0) = \int_D \psi_i(\mathbf{x}) G_{ij}(\mathbf{x}, \mathbf{x}_0)\, \mathrm{d}S(\mathbf{x}) \tag{2.1}$$

$$(\mathbf{K}_D \boldsymbol{\psi})_j(\mathbf{x}_0) = \int_D \psi_i(\mathbf{x}) T_{ijk}(\mathbf{x}, \mathbf{x}_0) n_k(\mathbf{x})\, \mathrm{d}S(\mathbf{x}), \tag{2.2}$$

where $\boldsymbol{\psi}$ is a vector field on D, and $\mathbf{G}$ and $\mathbf{T}$ are the Green's functions of a Stokeslet

and stresslet, respectively (Pozrikidis 1992). These Green's functions, in the presence of the periodic velocity boundary conditions used here, can be calculated by the Ewald sum (Hashimoto 1959). The derivation of the system BIEs follows the standard procedure that first utilizes the Lorenz reciprocal theorem and then applies a limiting process of letting the target point $\mathbf{x}_0$ approach a flow interface (i.e., any RBC, platelet or wall surface). The resulting equations can be written in a block format

$$\begin{pmatrix} \mathbf{A}_{CC} & \mathbf{A}_{CP} & \mathbf{A}_{CW} \\ \mathbf{A}_{PC} & \mathbf{A}_{PP} & \mathbf{A}_{PW} \\ \mathbf{A}_{WC} & \mathbf{A}_{WP} & \mathbf{A}_{WW} \end{pmatrix} \begin{pmatrix} \mathbf{u}_C \\ \boldsymbol{\psi}_P \\ \mathbf{f}_W \end{pmatrix} = \begin{pmatrix} \mathbf{b}_C \\ \mathbf{b}_P \\ \mathbf{b}_W \end{pmatrix}, \tag{2.3}$$

where C denotes red blood cells, P for platelets, and W for walls. The $\mathbf{u}_C$ is the surface moving velocity of RBCs, $\mathbf{f}_W$ is the hydrodynamic friction force on the vessel walls, and $\boldsymbol{\psi}_P$ is a fictitious double-layer density on the platelet surface that relates to the platelets' rigid-body velocity. The sub-block linear operators are

$$\mathbf{A}_{CC} = \tfrac{1+\lambda}{2}\mathbf{I} - \tfrac{1-\lambda}{8\pi}\mathbf{K}_{CC} \quad \mathbf{A}_{CP} = \tfrac{1}{8\pi}\mathbf{K}_{CP} \quad \mathbf{A}_{CW} = \tfrac{1}{8\pi\mu}\mathbf{N}_{CW} \tag{2.4}$$

$$\mathbf{A}_{PC} = -\tfrac{1-\lambda}{8\pi}\mathbf{K}_{PC} \quad \mathbf{A}_{PP} = \tfrac{1}{2}\mathbf{I} + \tfrac{1}{8\pi}\mathbf{K}_{PP} + \sum_{\beta=1}^{6}(\mathbf{q}''^{\beta}, \cdot)\mathbf{q}''^{\beta} \quad \mathbf{A}_{PW} = \tfrac{1}{8\pi\mu}\mathbf{N}_{PW} \tag{2.5}$$

$$\mathbf{A}_{WC} = -\tfrac{1-\lambda}{8\pi}\mathbf{K}_{WC} \quad \mathbf{A}_{WP} = \tfrac{1}{8\pi}\mathbf{K}_{WP} \quad \mathbf{A}_{WW} = \tfrac{1}{8\pi\mu}\mathbf{N}_{WW}, \tag{2.6}$$

where λ is the ratio between the viscosity of the hemoglobin solution enclosed by the RBC membrane and the surrounding plasma's viscosity μ. Every boundary integral operator carries two subscripts to denote the two sub-systems between which the hydrodynamic interaction occur. For example,

$$(\mathbf{N}_{CW}\mathbf{f}_W)_j(\mathbf{x}_0) = \int_W f_{W\,i}(\mathbf{x}) G_{ij}(\mathbf{x}, \mathbf{x}_0)\, \mathrm{d}S(\mathbf{x}) \tag{2.7}$$

evaluates the velocity induced at a point $\mathbf{x}_0$ on any RBC surface (C) by a force distribution $\mathbf{f}_W$ on the vessel walls (W). The six surface vectors $\mathbf{q}''^{(\beta)}$ $(1 \le \beta \le 6)$ are defined for each rigid platelet and each represents one of the six orthonormal rigid-body motions (Pozrikidis 1992). Once $\boldsymbol{\psi}_P$ is solved, the velocity of the platelet is obtained via a projection

$$\mathbf{u} = \sum_{\beta=1}^{6} \left\langle \boldsymbol{\psi}, \mathbf{q}''^{(\beta)} \right\rangle \mathbf{q}''^{(\beta)}. \tag{2.8}$$

The right-hand sides are

$$\mathbf{b}_C = -\tfrac{1}{8\pi\mu}\mathbf{N}_{CC}\left[\!\left[\mathbf{f}\right]\!\right]_C + \langle \mathbf{u} \rangle \tag{2.9}$$

$$\mathbf{b}_P = -\tfrac{1}{8\pi\mu}\mathbf{N}_{PC}\left[\!\left[\mathbf{f}\right]\!\right]_C + \langle \mathbf{u} \rangle \tag{2.10}$$

$$\mathbf{b}_W = -\tfrac{1}{8\pi\mu}\mathbf{N}_{WC}\left[\!\left[\mathbf{f}\right]\!\right]_C + \langle \mathbf{u} \rangle, \tag{2.11}$$

where $\left[\!\left[\mathbf{f}\right]\!\right]_C$ is the total hydrodynamic force density acting on the RBC surface and hence can be explicitly calculated from the surface deformation. Let $\lambda_{1,2}$ be the principle

stretches of the RBC membrane, we define the two strain invariants

$$I_1 = \lambda_1^2 + \lambda_2^2 - 2 \qquad I_2 = \lambda_1^2\lambda_2^2 - 1, \tag{2.12}$$

and the density of the strain energy is (Skalak *et al.* 1973; Pozrikidis 2005)

$$W_S = \frac{E_S}{4}(\frac{1}{2}I_1^2 + I_1 - I_2) + \frac{E_D}{8}I_2^2, \tag{2.13}$$

where E_S is the shear modulus, and E_D is a dilatation modulus to approximately enforce the membrane's in-plane incompressibility. With the surface of every RBC discretized into a linear triangular mesh elements shown in Figure 1, W_S can be computed using the standard piecewise linear finite element. The bending energy is calculated based on the dihedral angles between adjacent triangular elements (Li *et al.* 2005; Dao *et al.* 2006):

$$W_B = \sum_e E_B \frac{l_e^2}{A_e}(1 - \cos\beta_e), \tag{2.14}$$

where E_B is the bending stiffness, e is the common edge shared by any two adjacent triangles, l_e is the edge length, A_e is the average of the areas of the two triangles, and β_e is the change in the dihedral angle at e due to deformation. The residual force is directly calculated by the virtual work principle as the first variation of W_S and W_B so that for each vertex α,

$$[\![\mathbf{f}]\!]_\alpha = \frac{1}{A_\alpha}\frac{\partial(W_S + W_B)}{\partial \mathbf{x}_\alpha}, \tag{2.15}$$

where A_α is one third of the sum of the area of all the triangles that surround α.

The governing equation, after being discretized using the standard linear boundary element method, becomes a linear equation about $\mathbf{u}_C$, $\boldsymbol{\psi}_P$ and $\mathbf{f}_W$, and is solved by a matrix-free GMRES solver without explicitly forming the dense matrix. The matrix-vector multiplications during the iterative solutions are performed implicitly via directly computing the surface integrals at collocation points, which is accelerated by the smooth particle Ewald sum method (SPME) with $O(N \log N)$ computational cost where N is the total number of surface mesh points (Saintillan *et al.* 2005; Zhao *et al.* 2010).

Following (Pozrikidis 2005), all quantities are nondimensionalized by: (1) the equivalent cell radius $a^* \approx 2.82\mu$m, where a red cell has the same volume as that of a sphere of radius a^*; (2) a reference shear rate $\dot{\gamma}^* = 100\text{s}^{-1}$, which gives a reference velocity $U^* = \dot{\gamma}^* a^* = 0.282$mm/s; (3) plasma viscosity $\mu^* = 1.2\times10^{-3}\text{kg}\cdot\text{m}^{-1}\cdot\text{s}^{-1}$. The cell membrane has shear modulus $E_S^* = 4.2\times10^{-6}$N/m and bending stiffness $E_B^* = 1.8\times10^{-19}\text{N}\cdot\text{m}$, which become $E_S = E_S^*/(\mu^*\dot{\gamma}^* a^*) = 12.4$ and $E_B = E_B^*/(\mu^*\dot{\gamma}^* a^{*3}) = 0.067$ when nondimensionalized. The membrane dilatational modulus is $E_D = 10E_S$ as a penalty parameter, and the local area change remains below 5% in all our simulations.

Most of our flow simulations have a dimensionless computational domain of length $L = 16$ in the flow direction and a height of $H = 12$. The spanwise size of the domain is 9, which is more than 3 times the RBC diameter, thus allowing fully three-dimensional flow development. Although the normal range of human body hematocrit is 40% to 50%, the local hematocrit drops significantly in small vessels and is only about 40% of the body average at 30μm vessel diameter (Lipowsky *et al.* 1978, 1980). Hence the mean hematocrit $\langle H_t \rangle$ in this study is chosen to be between 0.15 and 0.25. With an initial random disposition of undeformed red cells, more than 50 flow-through times $(L/\langle u \rangle)$ are typically necessary to establish steady-state cellular distributions. At $\langle u \rangle =$

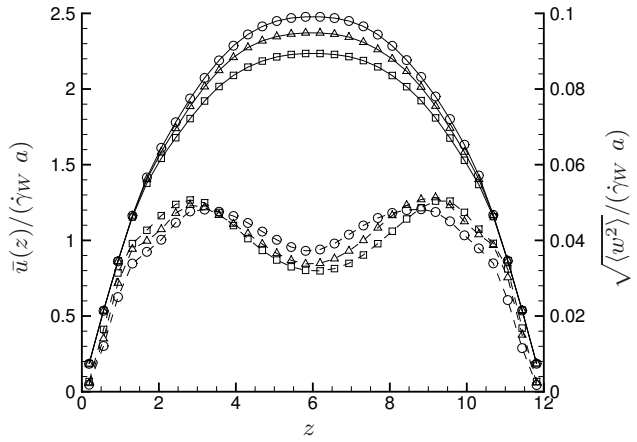

FIGURE 2. Profiles of mean axial velocity (solid line) and wall normal velocity fluctuation (dashed lines) at $\langle H_t \rangle = 20\%$ and $\langle u \rangle = 6$ ◘ , 12 △ , and 24 ○ .

12, this corresponds to a relaxation time of about 70, which is in line with the time scale $(H/a)^3 a/\langle u \rangle = 144$ for rigid particulate flow to reach steady state (Nott & Brady 1994).

3. Results

3.1. *Velocity profiles*

Figure 2 shows the profiles of the mean axial velocity and the root mean square (RMS) of wall normal velocity fluctuations. In the cell-free layer, the mean velocity follows that of the Poiseuille flow, but becomes more "blunt" than the parabolic profile inside the core cellular flow region. The degree of blunting becomes smaller at higher shear rate due to shear thinning (Chien *et al.* 1966).

Qualitatively, we find RBCs next to the cell-free Fahraeus–Lindquist zone are aligned with flow, and their equilibrium position is the result of the balance between wall lifting and the cell–cell repulsions. This layered structure is relatively stable, while there are strong normal velocity fluctuations right inside this layer (i.e., toward the channel center), as shown by the dashed lines in Figure 2. The wall shear rates $\dot{\gamma}_W$ are between 100s^{-1} and 1300s^{-1} within the physiological range in microvasculature. The elongation and flow alignment of RBCs appear more significant with increasing flow rate, and the RMS of velocity fluctuations scales linearly with $\dot{\gamma}_W$.

3.2. *Characteristics of wall normal velocity fluctuations*

The time scale of the wall normal velocity fluctuations is characterized by the normalized autocorrelation of Lagrangian tracers, which are placed randomly in the extracellular region and then passively convected by flow. The channel is divided equally into 24 intervals in the z direction, and for spatial binning the correlation $w(t)w(t+\Delta t)$ is assigned to the z-interval that the tracer lies within at time t. The normalized autocorrelation curves at different channel heights are shown in Figure 3. At $z = 1$ and 2 outside of the core flow region (empirically defined as $|z - H/2| < H/4$), the curves overlap well when time is scaled by $\dot{\gamma}_W$. Since the local shear rate in the core region varies superlinearly with $\dot{\gamma}_W$ due to shear thinning, the correlation curves at $z = H/2$ (top of Figure 3) fail to overlap with the same rescaling of time. The overlapping, however, can be recovered if we instead

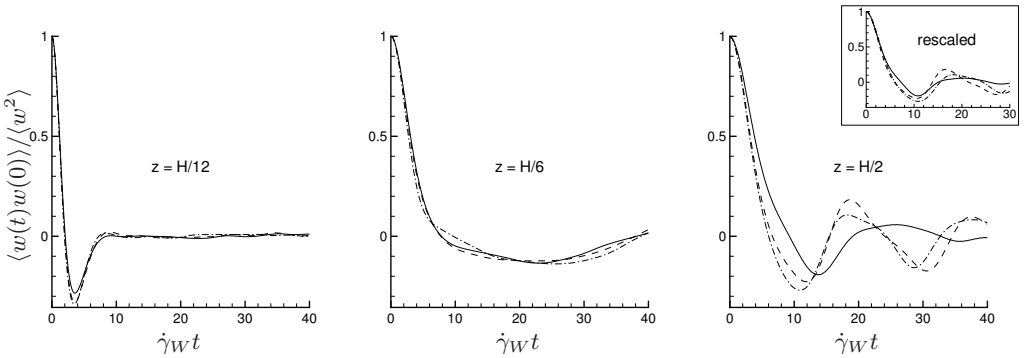

FIGURE 3. The autocorrelation of Lagrangian tracers at different channel heights. $\langle u\rangle = 6$ ——, 12 – – – –, and 24 —·—. Inset on the top: time rescaled by the effective shear rate in the core flow region.

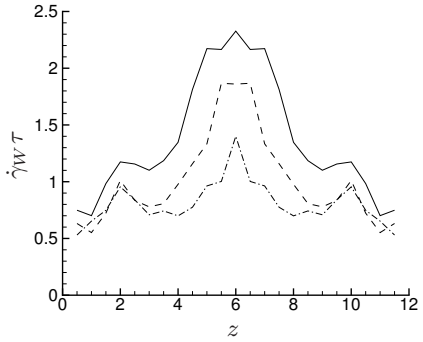

FIGURE 4. Profile of tracer particles' wall normal velocity decorrelation time $\tau = \int_0^\infty \langle w(t)w(0)\rangle\,\mathrm{d}t/\langle w^2\rangle$ at $\langle u\rangle$= 6 ——, 12 – – – –, 24 —·—.

scale t by an effective shear rate defined to be proportional to $(u|_{z=H/2} - u|_{z=H/4})/(H/4)$, as shown by the inset in the same figure.

The decorrelation time, defined as $\tau = \int_0^\infty \langle w(t)w(0)\rangle\,\mathrm{d}t/\langle w^2\rangle$, is shown in Figure 4. At the same wall shear rate, τ increases with decreasing local shear rate, reaching its maximum at the channel center. The local peak of τ at $z = 2$ appears to be due to the relatively stable flow-aligned cellular structure next to the cell-free layer. Due to shear thinning, the normalized decorrelation time $\dot{\gamma}_W\tau$ decreases as $\dot{\gamma}_W$ increases. We note that since the shear-induced wall normal diffusivity $D_\perp \propto \langle w^2\rangle\tau$, with the term $\langle w^2\rangle \sim \dot{\gamma}_W^2$ across the channel height (cf. Figure 2), $D_\perp$ must scale sublinearly with $\dot{\gamma}_W$ due to the superlinear decay of τ (i.e., $\dot{\gamma}_W\tau$ decreases as $\dot{\gamma}_W$ increases). *Note that it follows then from dimensional analysis that the diffusivity must depend on the elastic properties of the RBC membrane. We have verified this via additional computations that we discuss in the last section of this brief.*

Figure 5 shows the mean square displacement $\langle\Delta z^2\rangle(t) = \langle[z(t) - z(0)]^2\rangle$ of tracers as well as of platelets in the fully coupled simulations. The slope $\frac{1}{2}\mathrm{d}\langle\Delta z^2\rangle(\tau)/\mathrm{d}\tau$ gives the diffusivity $D_\perp$. We have found only minor variations of spreading speed in the core region because during the spreading process, tracer particles sample velocity fluctuations at different z planes and the spread width is already $O(1)$ and comparable to the channel size when the asymptotic linear spreading rate is established. Therefore $\langle\Delta z^2\rangle$ averaged

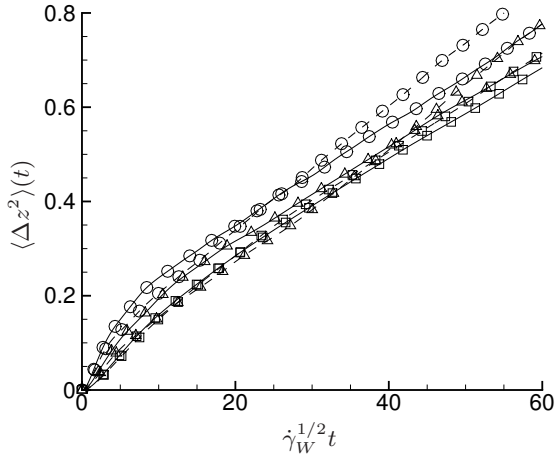

FIGURE 5. On top: mean square displacement in z-direction of tracers $\langle u \rangle = 6$ ▫ , 12 △ , and 24 ○ . The statistics is taken for $3 < z < 9$, thus excluding the cell-depleted zone. The solid lines are for tracer particles, and dashed lines for platelets.

in the whole core region is plotted for clear visualization. Figure 5 shows that a good fit can be obtained by an empirical scaling of time $\dot{\gamma}_W^{1/2} t$. The scaling $D_\perp \sim \dot{\gamma}_W^{1/2}$ confirms our previous argument of the sublinear scaling of $D_\perp$ with $\dot{\gamma}_W$ due to shear thinning. Of course, we note the power law fitting as well as the 1/2 exponent are purely empirical.

In our fully-coupled RBC/platelet simulations, the axial velocity of platelets, as well as the RMS z-velocity fluctuation, does not differ significantly from tracers in flows without platelets (not shown), which confirms our assumption that the existence of platelets does not change the overall characteristics of the flow. Figure 5 shows that spreading curves of platelets (plotted in dashed lines) are quantitatively similar to those of tracer particles, and we conclude that in the core region $D_\perp$ of platelets also scales with $\dot{\gamma}_W^{1/2}$. This result agrees with the experimental findings by Aarts et al (Aarts *et al.* 1986), where the effective diffusivity of platelets was found to obey a power law with shear rate with exponent less than 1. They empirically fit this exponent as a quadratic polynomial of hematocrit, which gives a value 0.52 for $H_t = 0.2$ as in our simulation, and 0.64 for $H_t = 0.35$, which is the maximal local hematocrit occurring at the channel center line.

3.3. *Platelet margination*

From the platelet trajectories in the z direction in one simulation as shown in Figure 6, the trend of migration from the core region toward the wall is clear. The margination appears irreversible once the platelets are expelled into the cell depleted layer, where the very small velocity fluctuations make it difficult for the platelet to re-enter the core region. The platelet number density profile at $t = 190$ is shown, where for the spatial average the channel is divided into 24 slices in z direction. Compared with the density profile at an earlier time $t = 55$, more than half of the platelets have moved to the cell-free layer and are trapped there. We note that the asymmetric concentration profile is caused by the bias in the initial platelet distribution that is difficult to control precisely when they are released near the center.

The time evolution of RMS distance of platelets from the center line is shown in Figure 7. The time axis is scaled by the mean velocity, and the plot shows that the velocity of platelet spreading is $O(10^{-3})$ of the mean convection. Thus for a platelet migrating from

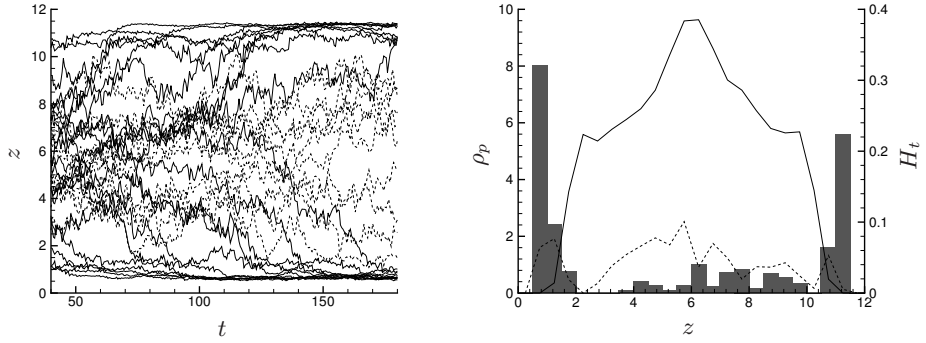

FIGURE 6. Left: platelet trajectories in wall normal direction. Right: the black bar is the platelet density profile at $t = 190$; for comparison the dashed line is the platelet density profile at an earlier time $t = 55$. The solid line is the RBC hematocrit profile. $\langle u \rangle = 24$ and $\langle H_t \rangle = 0.2$.

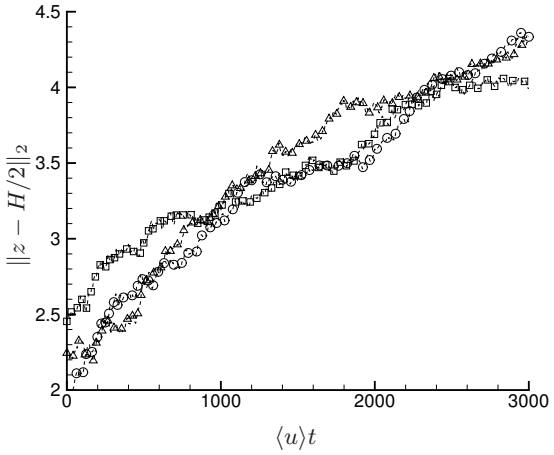

FIGURE 7. The RMS distance between platelets and channel center line. $\langle u \rangle = 6$ □ , 12 △ , 24 ○ .

the center line toward the wall, it will on average travel $O(10)$mm in the streamwise direction for a channel height of $H = 34\mu$m. This convection length is 20 times that of the average blood vessel branch (about 500μm) at this diameter (Lapi *et al.* 2008). Therefore, the vessel branches will play a role in determining the equilibrium platelet concentration profile in the actual microvascular network.

4. Conclusion and future plan

In summary, we have studied the margination of platelets in micro-channels by direct numerical simulation that fully resolves the hydrodynamic interactions in the system. It is demonstrated that it is the wall normal velocity fluctuations in the core flow region that expel the platelets toward the wall, and the migration is a shear-induced diffusional process where the effective diffusivity scales sublinearly with the wall shear rate as a result of flow shear thinning.

Our DNS has demonstrated that the velocity fluctuation in the RBC channel flow dominates the lateral dispersion of small particles. The question remains how the shape of RBCs and their membrane's mechanical properties affect the dispersion. This is of

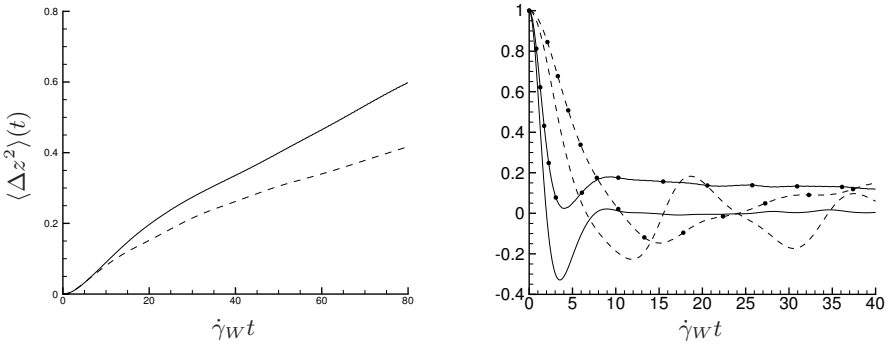

FIGURE 8. Left: mean square displacement in z-direction of tracers for normal RBCs (– – – –) and RBCs with stiffened membrane (———). Right: wall normal velocity autocorrelation at $z = H/12$ (———) and $z = H/2$ (– – – –). The curves with symbols are with the stiffened membranes.

practical importance as both can differ significantly from those of normal RBCs from gene mutation (sickle cell disease) or exogenous infection (malaria). For an initial investigation, we repeat the simulation at $H_t = 20\%$ and $\langle u \rangle = 12$, but with a membrane bending stiffness four times that used previously. Figure 8 shows that the wall normal velocity decorrelation time increases with membrane stiffening, and as a result, the diffusivity of tracer particles increases by about 50%.

An investigation is currently under way to systematically study the dependence of the shear-induced diffusivity of platelets on shear rate and membrane parameters in the more controllable simple shear flow environment.

We thank the U.S. Army High Performance Computing Research Center (AHPCRC) for supporting this work.

REFERENCES

AARTS, P. A., STEENDUK, P., SIXMA, J. J. & HEETHAAR, R. M. 1986 Fluid shear as a possible mechanism for platelet diffusivity in flowing blood. *J. Biomech.* **19** (10), 799–805.

CHIEN, S., USAMI, S., TAYLOR, H. M., LUNDBERG, J. L. & GREGERSEN, M. I. 1966 Effects of hematocrit and plasma proteins on human blood rheology at low shear rates. *J. Appl. Physiol.* **21** (1), 81–87.

DAO, M., LI, J. & SURESH, S. 2006 Molecularly based analysis of deformation of spectrin network and human erythrocyte. *Mater. Sci. Engrg. C* **26**, 1232–1244.

ECKSTEIN, E. C., BAILEY, D. G. & SHAPIRO, A. H. 1977 Self-diffusion of particles in shear flow of a suspension. *J. Fluid Mech.* **79** (1), 191–208.

FAHRAEUS, R. & LINDQVIST, T. 1931 The viscosity of blood in narrow capillary tubes. *Am. J. Physiol.* **96**, 562–568.

HASHIMOTO, H. 1959 On the periodic fundamental solutions of the stokes equations and their application to viscous flow past a cubic array of spheres. *J. Fluid Mech.* **5**, 317–328.

KRATZ, A., FERRARO, M., SLUSS, P. M. & LEWANDROWSKI, K. B. 2004 Laboratory reference values. *N. Engl. J. Med.* **351**, 1548–1563.

Lapi, D., Marchiafava, P. L. & Colantuoni, A. 2008 Geometric characteristics of arterial network of rat pial microcirculation. *Vasc. Res.* **45**, 69–77.

Leighton, D. & Acrivos, A. 1987 The shear-induced migration of particles in concentrated suspensions. *J. Fluid Mech.* **181**, 415–439.

Li, J., Dao, M., Lim, C. T. & Suresh, S. 2005 Spectrin-level modeling of the cytoskeleton and optical tweezers stretching of the erythrocyte. *Biophs. J.* **88**, 3707–3719.

Lipowsky, H. H., Kovalcheck, S. & Zweifach, B. W. 1978 The distribution of blood rheological parameters in the microvasculature of cat mesentery. *Circ. Res.* **43** (5), 738–749.

Lipowsky, H. H., Usami, S. & Chien, S. 1980 *In Vivo* measurements of apparent viscosity and microvessel hematocrit in the mesentery of the cat. *Microvasc. Res.* **19**, 297–319.

Michelson, A. 2006 *Platelets, Second Edition*. Academic Press.

Nott, P. R. & Brady, J. F. 1994 Pressure-driven flow of suspensions: simulation and theory. *J. Fluid Mech.* **275**, 157–199.

Pozrikidis, C. 1992 *Boundary Integral and Singularity Methods for Linearized Viscous Flow*. Cambridge: Cambridge University Press.

Pozrikidis, C. 2003 Numerical simulation of the flow-induced deformation of red blood cells. *Annals of Biomedical Engineering* **31**, 1194–1205.

Pozrikidis, C. 2005 Axisymmetric motion of a file of red blood cells through capillaries. *Phys. Fluids* **17**, 031503.

Saintillan, D., Darve, E. & Shaqfeh, E. S. G. 2005 A smooth particle-mesh Ewald algorithm for Stokes suspension simulations: The sedimentation of fibers. *Phys. Fluids* **17**, 033301.

Skalak, R., Tözeren, A., Zarda, P. R. & Chien, S. 1973 Strain energy function of red blood cell membranes. *Biophs. J.* **13**, 245.

Tilles, A. W. & Eckstein, E. C. 1987 The near-wall excess of platelet-sized particles in blood flow: Its dependence on hematocrit and wall shear rate. *Microvasc. Res.* **33**, 211–223.

Yeh, C. & Eckstein, E. C. 1994 Transient lateral transport of platelet-sized particles in flowing blood suspensions. *Biophs. J.* **66**, 1706–1716.

Zhao, H., Isfahani, A. H. G., Olson, L. & Freund, J. B. 2010 A spectral boundary integral method for micro-circulatory cellular flows. *J. Comput. Phys.* **229** (10), 3726–3744.